Journal of Alloys and Compounds 767 (2018) 1141–1154

Contents lists available at ScienceDirect

Journal of Alloys and Compounds

journal homepage: http://www.elsevier.com/locate/jalcom

# Chemo-elastic phase-field simulation of the cooperative growth of mutually-accommodating Widmanstätten plates

P.G. Kubendran Amos [a, *, 1], Ephraim Schoof [a, b, 1], Daniel Schneider [a, b], Britta Nestler [a, b]

[a] Institute of Applied Materials (IAM-CMS), Karlsruhe Institute of Technology (KIT), Strasse am Forum 7, 76131 Karlsruhe, Germany
[b] Institute of Digital Materials Science (IDM), Karlsruhe University of Applied Sciences, Moltkestr. 30, 76133 Karlsruhe, Germany

ARTICLE INFO

*Article history:*
Received 8 May 2018
Received in revised form
10 July 2018
Accepted 11 July 2018
Available online 18 July 2018

*Keywords:*
Widmanstätten ferrite
Self-accommodating plates
Phase-field model
Chemo-elastic transformation
Austenite decomposition
CALPHAD
Steel

ABSTRACT

A comprehensive understanding of the phase transformations is of primary importance to optimize the properties of a material. In the present study, a novel and thermodynamically consistent chemo-elastic multiphase-field model is formulated to simulate phase transformations which yield unique needle-like patterns, referred to as Widmanstätten structure. Owing to the critical role of the curvature in the growth of the Widmanstätten structure, the model is devised to recover the sharp interface solutions, despite the introduction of a diffuse interface. This condition is fulfilled by formulating the chemical and the elastic driving force based on the grand potential density and the mechanical jump conditions, respectively. Additionally, to render a quantitative chemical driving force, parameters from CALPHAD-database (TCFE8) are incorporated. The current work, through the multicomponent multiphase-field simulations, shows that at high temperatures, when the chemical driving force is insufficient to actuate the growth of a plate, the Widmanstätten structure evolves by the co-operative growth of self-accommodating plates. Furthermore, the growth of a single Widmanstätten plate at low temperature is also simulated, and the growth kinetics of the transformations are verified through existing analytical predictions.



## 1. Introduction

Properties of a material, which determine its applicability, are substantially influenced by its constituent phases. Thus, manufacturing techniques are meticulously devised to render necessary phases, while equally circumventing the formation of certain other phases that are detrimental to the desired properties. Particularly in steels, owing to its adverse influence on the toughness of the material, the formation of lath-shaped ferrite, commonly known as Widmanstätten ferrite, is not favored [1]. However, it has also been identified that a large volume fraction of Widmanstätten ferrite increases the yield strength [2,3]. The potential appearance of Widmanstätten ferrite during manufacturing processes, like hot rolling [4] and welding [5], and its significant influence on the mechanical properties, makes theoretical or experimental attempts to understand this transformation interesting for both engineers and material scientists.

The decomposition of austenite involves a spectrum of phase transformations which are predominantly regulated by composition and temperature [6,7]. The diffusional or reconstructive transformation, which accounts for the formation of pearlite and pro-eutectoid ferrite, and which is governed by the diffusion of carbon and other alloying elements, renders a convincing description for the growth of Widmanstätten ferrite. Accordingly, it is postulated that the broad-faces of this lath-shaped ferrite consist of structural ledges with erratically distributed risers [8,9]. While the structural ledges make the broad-faces sessile, the risers, being incoherent, enable the diffusion of the atoms and thereby facilitate the lateral expansion of the Widmanstätten ferrite. Furthermore, the edge is considered to be made of growth ledges with large incoherent risers which govern the growth of the Widmanstätten ferrite [10]. Based on this description of the interface, theoretical studies on Widmanstätten ferrite often assume fully- or semi-coherent broad-faces and an incoherent edge [11,12]. Despite TEM (Transmission Electron Microscopy) investigation of the interfaces [13], a lack of experimental support to the description of the edge [14] and the formation of surface relief [15,16] posits a contending view to this understanding of the growth of Widmanstätten ferrite.

* Corresponding author.
*E-mail address:* prince.amos@kit.edu (P.G. Kubendran Amos).
[1] The authors contributed equally.

https://doi.org/10.1016/j.jallcom.2018.07.138

The shape change involved in the growth of Widmanstätten ferrite is revealed by the formation of well-defined surface distortions. The surface relief, which is usually associated with the diffusionless or displacive transformation, presents the plausibility of a contrasting description for the growth of this lath-shaped ferrite [17,18]. A crystallographic analysis investigating the habit plane and orientation relationship of Widmanstätten ferrite relates the formation of the surface relief to the invariant-plane strain [19]. Although this study concedes that the transformation mechanism cannot entirely be determined from the crystallographic analysis, it concludes by stating that 'crystallographic theory, provide the strongest evidence that the growth mechanism of Widmanstätten ferrite is martensite in character'. Furthermore, the dilatometric study on isothermal phase-transformations of steel claims that the strain accompanying the growth of Widmanstätten ferrite contributes to the observed dilatation [20]. Evidently, this study reveals three distinct C-curves in the TTT (time-temperature-transformation) plot, indicating the difference in the transformation mechanism governing the growth of pearlite and Widmanstätten ferrite. Several extensive microscopic investigations by Ohmori et al. propose displacive growth of Widmanstätten ferrite [21–24]. The diffusionless transformation of the phases like martensite, which is accompanied by the invariant-plane strain, is influenced by pre-existing strain induced by deformation [25–27]. An analysis of the phase transformation on deformed austenite reveals a decreased amount of Widmanstätten ferrite [28]. This mechanical stabilization of the lath-shaped ferrite substantiates the displacive mechanism of growth. In addition to the recent report on dislocation densities [29], the lack of any austenite decomposition in a small temperature range between the Widmanstätten start temperature and the lowest temperature at which allotriomorphs or pearlite is identified [30], indicates a shift in the transformation mechanism from the reconstructive to the diffusionless transformation. Despite the displacive nature of the transformation, considering the temperature at which Widmanstätten ferrite grows, it is maintained that the equi-partitioning of carbon occurs during the evolution. It is furthermore asserted that the growth kinetics of the transformation are governed by this carbon diffusion. Thus, although para-equilibrium is established in systems comprising substitutional alloying elements, both the theories concur on the equi-partitioning of carbon in a binary Fe-C system. Amidst the ongoing contention between these views, the present work adopts the displacive theory for the simulation of Widmanstätten ferrite owing to its substantial role in well-established theoretical models of industrial applications [31,32] and archaeological interpretation [33].

With the progressive availability of computational resources, numerical techniques have proven to be a critical tool in capturing the intricate aspects of phase transformations. One such computational approach, referred to as phase-field modelling, has grown to be a pivotal method for simulating complex microstructures and understanding its evolution mechanism [34]. In this approach, the interface separating two bulk phases is replaced with a smoothly varying function called phase-field. Thus, the evolution of this function translates directly to the phase transformation observed in the simulation. Several theoretical analyses of Widmanstätten ferrite involving phase-field models have been increasingly reported [35–40]. However, most of these studies incline towards the reconstructive mechanism of transformation, and thereby assume coherent and incoherent interfaces along the broad-faces and the edge of the Widmanstätten ferrite, respectively. Accordingly, these studies employ anisotropy in the interfacial energy to achieve the lath morphology. The numerical instability introduced by the strong anisotropy in the interfacial energy and the need for a regularization term has been discussed recently in Ref. [41]. Different from these analyses and adhering to the displacive theory, Widmanstätten structures has recently been simulated by introducing elasticity [38]. Although this approach was extended to simulate Widmanstätten ferrite [39], one critical aspect of the displacive theory remains un-addressed in all the aforementioned phase-field studies. The strain energy induced during the displacive growth of martensite, in addition to the plastic relaxation, is minimized by the co-operative 'back-to-back' growth of lath of near identical orientation relation [42]. Based on the partial-dislocation degeneracy in the martensite transformation [43,44], which enables the co-operative growth of the plates, the plausibility of such self-accommodating growth of Widmanstätten ferrite is postulated [45]. Subsequently, numerous experimental investigations, including TEM observation [46], have been reported in favor of the co-operative growth of mutually-accommodating Widmanstätten ferrite laths [47–50]. Although a phase-field study on the plastic relaxation accompanying the Widmanstätten ferrite has been reported [51], the co-operative growth of the laths has not been presented yet. Thus, a thermodynamically consistent chemo-elastic multiphase-field model is formulated and employed in this study, to simulate the co-operative growth of mutually-accommodating Widmanstätten ferrite laths in the Fe-C binary system, while overlooking the contribution from the plastic relaxation.

## 2. Theoretical framework

### 2.1. Multiphase-field model

A multicomponent multiphase-field model, based on a free energy functional of Ginzburg-Landau type [52], is employed to simulate the isothermal chemo-mechanical transformation process. This functional is expressed as

$$\begin{aligned}\mathcal{F}(\phi,\nabla\phi,\overline{c},\overline{\varepsilon},\mathrm{T}) &= \mathcal{F}_{\mathrm{intf}}(\phi,\nabla\phi)+\mathcal{F}_{\mathrm{el}}(\phi,\overline{\varepsilon})+\mathcal{F}_{\mathrm{chem}}(\phi,\overline{c})\\ &= \int_{\mathrm{V}} \overline{\mathrm{W}}_{\mathrm{intf}}(\phi,\nabla\phi)+\overline{\mathrm{W}}_{\mathrm{el}}(\phi,\overline{\varepsilon})+\overline{\mathrm{W}}_{\mathrm{chem}}(\phi,\overline{c},\mathrm{T})\mathrm{dV},\end{aligned} \tag{1}$$

where $\phi(\boldsymbol{x},t)$ is a vector-valued continuous order parameter of $N$ components, whereby each order parameter, $\phi_\alpha(\boldsymbol{x},t)$, $\alpha = 1,\ldots,N$, represents the volume fraction of a particular phase $\alpha$. Furthermore, by adopting the approach of Nestler et al. [53,54], the phase-field model is equipped with sufficient degrees of freedom to enable the treatment of all plausible interfaces in a system of $N$ phases, and the interaction between two adjacent phases, separately. Thus, the interfacial free-energy density is written as the summation of the gradient and the potential energy density, $\overline{W}_{\mathrm{intf}}(\phi,\nabla\phi) = \varepsilon a(\phi,\nabla\phi) + \omega(\phi)/\varepsilon$, where $\varepsilon$ is a length parameter which governs the width of the diffuse interface. The gradient energy density

$$\varepsilon a(\phi,\nabla\phi) = \varepsilon \sum_{\alpha,\beta>\alpha} \gamma_{\alpha\beta}|\boldsymbol{q}_{\alpha\beta}|^2, \tag{2}$$

is expressed by the interfacial energy $\gamma_{\alpha\beta}$ and the normal vector to the $\alpha$–$\beta$ interface $\boldsymbol{q}_{\alpha\beta} = \phi_\alpha\nabla\phi_\beta - \phi_\beta\nabla\phi_\alpha$. Furthermore, in contrast to most phase-field models, the potential energy density

$$\frac{1}{\varepsilon}\omega(\phi) = \frac{16}{\varepsilon\pi^2}\sum_{\alpha,\beta>\alpha}\gamma_{\alpha\beta}\phi_\alpha\phi_\beta + \frac{1}{\varepsilon}\sum_{\alpha,\beta>\alpha,\delta>\beta}\gamma_{\alpha\beta\delta}\phi_\alpha\phi_\beta\phi_\delta, \tag{3}$$

is formulated by using an obstacle-type potential $\omega(\phi)$, which is set to $\infty$ if the $N$-tuple of the order parameters $\phi = \phi_1,..,\phi_N$ is not in the Gibbs simplex $\mathscr{G} = \left\{\phi\in\mathbb{R}^N : \sum_\alpha \phi_\alpha = 1, \phi_\alpha \geq 0\right\}$. Through the

additional higher order term $\propto \phi_\alpha\phi_\beta\phi_\delta$ in Eqn. (3), the formation of non-physical spurious, or third phases, in regions separating two phases is prevented. The role of this higher order term is extensively discussed in Ref. [55].

Under the constraint $\sum_\alpha \phi_\alpha = 1$, the variational approach yields the following condition at equilibrium

$$0 = \frac{\delta \mathcal{F}}{\delta \phi_\alpha} - \frac{1}{N}\sum_\beta \frac{\delta \mathcal{F}}{\delta \phi_\beta}, \quad \alpha = 1, \ldots, N. \tag{4}$$

Splitting this equilibrium conditions into dual interactions, the evolution equation of the order parameters involving chemical and elastic contribution, with the mobility $M_{\alpha\beta}$ of an $\alpha$–$\beta$ interface, reads

$$\frac{\partial \phi_\alpha}{\partial t} = -\frac{1}{\tilde{N}\varepsilon}\sum_{\beta\neq\alpha}^{\tilde{N}} \bar{M}_{\alpha\beta}\left(\frac{\delta \mathcal{F}_{\text{intf}}}{\delta \phi_\alpha} - \frac{\delta \mathcal{F}_{\text{intf}}}{\delta \phi_\beta} + \frac{8\sqrt{\phi_\alpha\phi_\beta}}{\pi}\left(\Delta^{\alpha\beta}_{\text{chem}} + \Delta^{\alpha\beta}_{\text{el}}\right)\right), \tag{5}$$

where $\tilde{N} \leq N$ is the number of active phases. In Eqn. (5), $\Delta^{\alpha\beta}_{\text{chem}}$ and $\Delta^{\alpha\beta}_{\text{el}}$ are the chemical and elastic driving forces, respectively, which are determined from appropriate functionals through $(\delta/\delta\phi_\alpha - \delta/\delta\phi_\beta)\mathcal{F}_{\text{chem}}$ and $(\delta/\delta\phi_\alpha - \delta/\delta\phi_\beta)\mathcal{F}_{\text{el}}$ [56,57]. Thus, the variational derivative of the total energy with respect to $\phi_\alpha$ can be represented by $\delta\mathcal{F}/\delta\phi_\alpha = (\partial/(\partial\phi_\alpha) - \nabla\cdot\partial/(\partial\nabla\phi_\alpha))\overline{W}$, where $(\nabla\cdot)$ denotes the divergence operator and $\overline{W}$ represents the chemical, elastic and interfacial energy contributions.

The chemical driving force for the evolution of the phases, which depend on the concentration and the temperature ($T$), is introduced by the chemical free-energy density $\overline{W}_{\text{chem}}$ written as

$$\overline{W}_{\text{chem}}(\phi, \bar{c}, T) = \sum_\alpha W^\alpha_{\text{chem}}(c^\alpha, T)\phi_\alpha. \tag{6}$$

In the above equation, the concentration for phase $\alpha$ is expressed as the tuple of $K-1$ independent concentrations $c^\alpha_i$, and the chemical free-energy density is represented by $W^\alpha_{\text{chem}}(c^\alpha, T)$. The derivative of this free energy density with respect to the $\phi_\alpha$, yields

$$\frac{\partial \overline{W}_{\text{chem}}}{\partial \phi_\alpha} = W^\alpha_{\text{chem}} + \sum_{i=1}^{K-1}\sum_\beta \frac{\partial W^\beta_{\text{chem}}}{\partial c^\beta_i}\frac{\partial c^\beta_i}{\partial \phi_\alpha}\phi_\beta. \tag{7}$$

A constraint on the concentration, expressed as $\bar{c}_i = \sum_\beta c^\beta_i \phi_\beta$, is introduced by the mass conservation, which translates to $\sum_\beta \phi_\beta \partial c^\beta_i/(\partial\phi_\alpha) = -c^\alpha_i$ upon derivation. By imposing this constraint under the consideration that $\partial W^1_{\text{chem}}/(\partial c^1_i) = \ldots = \partial W^N_{\text{chem}}/(\partial c^N_i) = \mu_i$, where $\mu_i$ is the chemical potential of the component $i$, Eqn. (7) reads

$$\begin{aligned}\frac{\partial \overline{W}_{\text{chem}}}{\partial \phi_\alpha} &= W^\alpha_{\text{chem}} + \sum_{i=1}^{K-1}\mu_i\sum_\beta \frac{\partial c^\beta_i}{\partial \phi_\alpha}\phi_\beta \\ &= W^\alpha_{\text{chem}} - \sum_{i=1}^{K-1}\mu_i c^\alpha_i.\end{aligned} \tag{8}$$

Since $W^\alpha_{\text{chem}} - \sum_{i=1}^{K-1}\mu_i c^\alpha_i = \Psi^\alpha_{\text{chem}}$, which is the grand potential density of $\alpha$ [58], the chemical driving force governing the evolution of the phases is expressed based on this grand potential densities as $\Delta^{\alpha\beta}_{\text{chem}} = [\![\Psi_{\text{chem}}]\!]^{\alpha\beta}$. For phase $\alpha$, this grand potential density reads

$$\Psi^\alpha_{\text{chem}}(T, \mu) = W^\alpha_{\text{chem}}(c^\alpha(T, \mu), T) - \sum_{i=1}^{K-1}\mu_i c^\alpha_i(T, \mu), \tag{9}$$

where $\mu$ is a continuous vector-valued chemical potential of $K-1$ independent potentials $\mu_i$. From the diffusion equation, the evolution of concentration fields for each of the $K-1$ independent variables, $c_i$, is determined from the gradient of the chemical potential $\mu_i$, through

$$\frac{\partial c_i}{\partial t} = \nabla\cdot\left(\sum_{j=1}^{K-1}\overline{\mathcal{M}}_{ij}(\phi)\nabla\mu_j\right) \tag{10}$$

$$\overline{\mathcal{M}}_{ij}(\phi) = \sum_{\alpha=1}^{N}\mathcal{M}^\alpha_{ij}\phi_\alpha. \tag{11}$$

In the above Eqn. (11), $\overline{\mathcal{M}}_{ij}$ encompasses the individual mobilities $\mathcal{M}^\alpha_{ij}$ which relate to the diffusivities in the particular phase $\alpha$. By combining the aforementioned governing equations, the evolution of the diffusion-potential field, which ultimately governs the transformation, is written as

$$\frac{\partial \mu_i}{\partial t} = \left[\sum_{\alpha=1}^{N}\phi_\alpha\frac{\partial c^\alpha_i(\mu, T)}{\partial \mu_j}\right]^{-1}_{ij}\left\{\nabla\cdot\sum_{j=1}^{K-1}\overline{\mathcal{M}}_{ij}(\phi)\nabla\mu_j - \sum_{\alpha=1}^{N}c^\alpha_i(\mu, T)\frac{\partial \phi_\alpha}{\partial t}\right\}. \tag{12}$$

The transformations based on the evolution of this diffusion-potential field are well-established and have already been successfully adopted in the simulation of solidification [59] and solid-state transformation [40]. Moreover, it has been recently shown that this approach reproduces the curvature-driven shape-instabilities while recovering the sharp interface solutions [60,61].

In addition to the chemical driving force, the phase transformations are often associated with the mechanical barriers in the form of elastic or plastic strains. As discussed in Sec. 1, it is postulated that the evolution of the Widmanstätten structure is predominantly accompanied by the elastic strains. In order to encompass the influence of the elasticity, the additional contribution $\Delta^{\alpha\beta}_{\text{el}}$ is included in the formulation of the phase-field model. Therefore, the derivative of the elastic free-energy density $\overline{W}_{\text{el}}(\phi, \bar{\varepsilon})$ is determined by adopting an approach presented in Refs. [62,63]. In this formulation, the stresses and the elastic driving force are calculated on the basis of mechanical jump conditions.

In a multiphase system, the homogenized normal vector $\boldsymbol{n}$ can be calculated by using a scalar field

$$M(\phi) = \sum_{\alpha<\beta}\phi_\alpha\phi_\beta \quad \Rightarrow \quad \boldsymbol{n}(M(\phi)) = \frac{\nabla M(\phi)}{|\nabla M(\phi)|}. \tag{13}$$

By incorporating the aforementioned definition of the normal $\boldsymbol{n}$, the stresses and strains are first transformed into an orthonormal basis $\boldsymbol{B} = \{\boldsymbol{n}, \boldsymbol{t}, \boldsymbol{s}\}$, which is further re-ordered in the Voigt notation as

$$\begin{aligned}\boldsymbol{\sigma}^\alpha_B(\boldsymbol{n}) &:= \left(\sigma_{nn}, \sigma_{nt}, \sigma_{ns}, \sigma^\alpha_{tt}, \sigma^\alpha_{ss}, \sigma^\alpha_{ts}\right)^T = \left(\boldsymbol{\sigma}_n, \boldsymbol{\sigma}^\alpha_t\right)^T \\ \boldsymbol{\varepsilon}^\alpha_B(\boldsymbol{n}) &:= \left(\varepsilon^\alpha_{nn}, 2\varepsilon^\alpha_{nt}, 2\varepsilon^\alpha_{ns}, \varepsilon_{tt}, \varepsilon_{ss}, 2\varepsilon_{ts}\right)^T = \left(\boldsymbol{\varepsilon}^\alpha_n, \boldsymbol{\varepsilon}_t\right)^T.\end{aligned} \tag{14}$$

Since the jump of the variables $\boldsymbol{\sigma}_n$ and $\boldsymbol{\varepsilon}_t$ vanishes according to the force balance $[\![\boldsymbol{\sigma}_n]\!] = 0$ and the Hadamard kinematic compatibility condition $[\![\boldsymbol{\varepsilon}_t]\!] = 0$, for an infinitesimal deformation on a singular plane [64], the continuous contributions of the stresses and strains are summarized in $\boldsymbol{\sigma}_n := (\sigma_{nn}, \sigma_{nt}, \sigma_{ns})$ and $\boldsymbol{\varepsilon}_t := (\varepsilon_{tt}, \varepsilon_{ss}, 2\varepsilon_{ts})$. Here, $\backslash llbracket\cdot\backslash rrbracket$ represents the jump of a variable

through the interface. The local strain $\boldsymbol{\varepsilon} = (\nabla \boldsymbol{u} + (\nabla \boldsymbol{u})^T)/2$ depends on the gradient of the displacement field, which is written as $(\nabla \boldsymbol{u})_{ij} = \partial u_i/\partial x_j$, using the Einstein summation convention. The variables $\boldsymbol{\sigma}_t^\alpha := (\sigma_{tt}^\alpha, \sigma_{ss}^\alpha, \sigma_{ts}^\alpha)$ and $\boldsymbol{\varepsilon}_n^\alpha := (\varepsilon_{nn}^\alpha, 2\varepsilon_{nt}^\alpha, 2\varepsilon_{ns}^\alpha)$ correspondingly summarize the discontinuous contributions of the stresses and strains. The superscript $\alpha$ implies that the variable is discontinuous, and therefore phase-dependent. Furthermore, the stiffness tensor, formulated in the basis $\boldsymbol{B}$, is divided into blocks for further calculations

$$\mathscr{C}_B^{\mathrm{v}} = \begin{pmatrix} \mathscr{C}_{nnnn} & \mathscr{C}_{nnnt} & \mathscr{C}_{nnns} & \mathscr{C}_{nntt} & \mathscr{C}_{nnss} & \mathscr{C}_{nnts} \\ \mathscr{C}_{ntnn} & \mathscr{C}_{ntnt} & \mathscr{C}_{ntns} & \mathscr{C}_{nttt} & \mathscr{C}_{ntss} & \mathscr{C}_{ntts} \\ \mathscr{C}_{nsnn} & \mathscr{C}_{nsnt} & \mathscr{C}_{nsns} & \mathscr{C}_{nstt} & \mathscr{C}_{nsss} & \mathscr{C}_{nsts} \\ \mathscr{C}_{ttnn} & \mathscr{C}_{ttnt} & \mathscr{C}_{ttns} & \mathscr{C}_{tttt} & \mathscr{C}_{ttss} & \mathscr{C}_{ttts} \\ \mathscr{C}_{ssnn} & \mathscr{C}_{ssnt} & \mathscr{C}_{ssns} & \mathscr{C}_{sstt} & \mathscr{C}_{ssss} & \mathscr{C}_{ssts} \\ \mathscr{C}_{tsnn} & \mathscr{C}_{tsnt} & \mathscr{C}_{tsns} & \mathscr{C}_{tstt} & \mathscr{C}_{tsss} & \mathscr{C}_{tsts} \end{pmatrix} = : \begin{pmatrix} \mathscr{C}_{nn} & \mathscr{C}_{nt} \\ \mathscr{C}_{tn} & \mathscr{C}_{tt} \end{pmatrix}, \tag{15}$$

with $\mathscr{C}_{nn}$ and $\mathscr{C}_{tt}$ representing the symmetrical matrices of dimension $3 \times 3$. The variables $\mathscr{C}_{nt}$ and $\mathscr{C}_{tn}$ are $3 \times 3$ matrices for which the condition $\mathscr{C}_{tn} = \mathscr{C}_{nt}^T$ is fulfilled. The same methodology is employed to construct the compliance tensor $\mathscr{S}^\alpha$. The calculation of the stresses is achieved by considering the potential with only continuous variables, which yields

$$\overline{\boldsymbol{\sigma}}_B = \underbrace{\begin{pmatrix} -\overline{\mathscr{T}}_{nn}^{-1} & -\overline{\mathscr{T}}_{nn}^{-1}\overline{\mathscr{T}}_{nt} \\ -\overline{\mathscr{T}}_{tn}\overline{\mathscr{T}}_{nn}^{-1} & \overline{\mathscr{T}}_{tt} - \overline{\mathscr{T}}_{tn}\overline{\mathscr{T}}_{nn}^{-1}\overline{\mathscr{T}}_{nt} \end{pmatrix}}_{\overline{\mathscr{C}}_B^{\mathrm{v}}(\phi)} \begin{pmatrix} \boldsymbol{\varepsilon}_n \\ \boldsymbol{\varepsilon}_t \end{pmatrix} + \underbrace{\begin{pmatrix} \overline{\mathscr{T}}_{nn}^{-1} & \boldsymbol{0} \\ \overline{\mathscr{T}}_{tn}\overline{\mathscr{T}}_{nn}^{-1} & -\boldsymbol{I} \end{pmatrix} \begin{pmatrix} \tilde{\boldsymbol{\chi}}_n \\ \tilde{\boldsymbol{\chi}}_t \end{pmatrix}}_{\tilde{\boldsymbol{\sigma}}_B}. \tag{16}$$

Here, $\tilde{\boldsymbol{\chi}}_n$ and $\tilde{\boldsymbol{\chi}}_t$ are the normal and tangential parts of the inelastic strains $\tilde{\boldsymbol{\varepsilon}}^\alpha$, which are respectively defined as

$$\tilde{\boldsymbol{\chi}}_n = \sum_\alpha (\tilde{\boldsymbol{\varepsilon}}_n^\alpha + \mathscr{T}_{nt}^\alpha \tilde{\boldsymbol{\varepsilon}}_t^\alpha)\phi_\alpha, \quad \tilde{\boldsymbol{\chi}}_t = \sum_\alpha \mathscr{T}_{tt}^\alpha \tilde{\boldsymbol{\varepsilon}}_t^\alpha \phi_\alpha, \tag{17}$$

respectively. Additionally, the locally averaged contributions of the proportionality matrix $\overline{\mathscr{T}}$, between continuous and discontinuous variables, are given by

$$\overline{\mathscr{T}}_{nn} := \sum_\alpha \mathscr{T}_{nn}^\alpha \phi_\alpha := -\sum_\alpha \left(\mathscr{C}_{nn}^\alpha\right)^{-1} \phi_\alpha \tag{18}$$

$$\overline{\mathscr{T}}_{nt} := \sum_\alpha \mathscr{T}_{nt}^\alpha \phi_\alpha := \sum_\alpha \left(\mathscr{C}_{nn}^\alpha\right)^{-1} \mathscr{C}_{nt}^\alpha \phi_\alpha \tag{19}$$

$$\overline{\mathscr{T}}_{tt} := \sum_\alpha \mathscr{T}_{tt}^\alpha \phi_\alpha := \sum_\alpha \left(\mathscr{C}_{tt}^\alpha - \mathscr{C}_{tn}^\alpha \left(\mathscr{C}_{nn}^\alpha\right)^{-1} \mathscr{C}_{nt}^\alpha\right) \phi_\alpha. \tag{20}$$

With the transformations $\overline{\mathscr{C}}^{\mathrm{v}}(\phi) = \boldsymbol{M}_\varepsilon^T \mathscr{C}_B^{\mathrm{v}}(\phi) \boldsymbol{M}_\varepsilon$ and $\tilde{\boldsymbol{\sigma}}^{\mathrm{v}}(\phi) = \boldsymbol{M}_\sigma^T \tilde{\boldsymbol{\sigma}}_B(\phi)$, the resulting stresses in the Voigt representation and in the Cartesian coordinate system are calculated by $\overline{\boldsymbol{\sigma}}^{\mathrm{v}}(\phi) = \overline{\mathscr{C}}^{\mathrm{v}}(\phi)\overline{\boldsymbol{\varepsilon}}^{\mathrm{v}} + \tilde{\boldsymbol{\sigma}}^{\mathrm{v}}(\phi)$, whereby the transformation matrices $\boldsymbol{M}_\varepsilon$ and $\boldsymbol{M}_\sigma$ are adopted from Ref. [62]. Upon transforming the resulting stress $\overline{\boldsymbol{\sigma}}^{\mathrm{v}}(\phi)$ into the matrix notation, the momentum balance $\nabla \cdot \overline{\boldsymbol{\sigma}}(\phi) = 0$ is solved for the displacement field $\boldsymbol{u}$. In bulk regions of an arbitrary phase $\alpha$, the stresses are calculated by $\sigma_{ij} = (\mathscr{C}^\alpha[\boldsymbol{\varepsilon} - \tilde{\boldsymbol{\varepsilon}}^\alpha])_{ij} = \mathscr{C}_{ijkl}^\alpha(\varepsilon_{kl} - \tilde{\varepsilon}_{kl}^\alpha)$. Finally, the derivative of the elastic free-energy density is given by $\partial \overline{W}_{\mathrm{el}}(\phi, \boldsymbol{\varepsilon}_B)/\partial\phi_\alpha = \partial \sum_\alpha p^\alpha(\boldsymbol{\sigma}_n, \boldsymbol{\varepsilon}_t)\phi_\alpha/\partial\phi_\alpha$, with

$$p^\alpha(\boldsymbol{\sigma}_n, \boldsymbol{\varepsilon}_t) = \frac{1}{2}\left(\begin{pmatrix} \boldsymbol{\sigma}_n \\ \boldsymbol{\varepsilon}_t \end{pmatrix} \cdot \begin{pmatrix} \mathscr{T}_{nn}^\alpha & \mathscr{T}_{nt}^\alpha \\ \mathscr{T}_{tn}^\alpha & \mathscr{T}_{tt}^\alpha \end{pmatrix} \begin{pmatrix} \boldsymbol{\sigma}_n \\ \boldsymbol{\varepsilon}_t \end{pmatrix}\right) - \left(\begin{pmatrix} \boldsymbol{\sigma}_n \\ \boldsymbol{\varepsilon}_t \end{pmatrix} \cdot \begin{pmatrix} \boldsymbol{I} & \mathscr{T}_{nt}^\alpha \\ \boldsymbol{0} & \mathscr{T}_{tt}^\alpha \end{pmatrix} \begin{pmatrix} \tilde{\boldsymbol{\varepsilon}}_n^\alpha \\ \tilde{\boldsymbol{\varepsilon}}_t^\alpha \end{pmatrix}\right) + \frac{1}{2}(\tilde{\boldsymbol{\varepsilon}}_t^\alpha \cdot \mathscr{T}_{tt}^\alpha \tilde{\boldsymbol{\varepsilon}}_t^\alpha). \tag{21}$$

The components of the proportionality matrix $\mathscr{T}^\alpha$ are expressed as

$$\mathscr{T}_{nn}^\alpha := -\mathscr{S}_{nn}^\alpha \tag{22}$$

$$\mathscr{T}_{nt}^\alpha := \mathscr{S}_{nn}^\alpha \mathscr{C}_{nt}^\alpha \tag{23}$$

$$\mathscr{T}_{tt}^\alpha := \mathscr{C}_{tt}^\alpha - \mathscr{C}_{tn}^\alpha \mathscr{S}_{nn}^\alpha \mathscr{C}_{nt}^\alpha. \tag{24}$$

### 2.2. CALPHAD-based chemical driving force

Despite the contention with regards to the transformation mechanism, it is unequivocally concurred that the growth kinetics of the Widmanstätten ferrite are governed by the carbon diffusion. Thus, in order to render the chemical driving force quantitatively, appropriate parameters from the CALPHAD database are incorporated. In a binary alloy system of components $i$ and $j$, the free energy $W_{chem}^\alpha$ of a phase $\alpha$, is expressed as

$$W_{chem}^\alpha(c_i, c_j, T) = c_i W_i(T) + c_j W_j(T) + RT[c_i \ln c_i + c_j \ln c_j], \tag{25}$$

where $W_i$ and $W_j$ are the respective free energies of the pure elements $i$ and $j$. The concentrations are included as the mole fractions of the components $i$ and $j$, $c_i$ and $c_j$, with $R$ and $T$ representing the universal gas constant and temperature in Kelvin, respectively. But in the Fe-C system, wherein the carbon atoms occupy the interstitial sites of the Fe lattice, two sub-lattices, $s_1$ and $s_2$, are considered to represent $W_{chem}^\alpha$ [65,66], which reads

$$W_{chem}^\alpha = Y_{Va}^{s_2} W_{Fe:Va} + Y_C^{s_2} W_{Fe:C} + RT[\tilde{a}^{s_2}(Y_C^{s_2} \ln Y_C^{s_2} + Y_{Va}^{s_2} \ln Y_{Va}^{s_2})] + Y_C^{s_2} Y_{Va}^{s_2} \bar{L}_{Fe:Va,C} + W_m^{mo}. \tag{26}$$

Here, in contrast to Eqn. (25), the concentration is expressed as site fractions, $Y_C^{s_2}$ and $Y_{Va}^{s_2}$, where $C$ and $Va$ are the components pertaining to the sub-lattice $s_2$. In a sub-lattice $s$, this site fraction of a component $i$ can be related to its mole fraction $c_i$ by $c_i = \sum a^s Y_i^s / \sum a^s (1 - Y_{Va}^s)$, where $a^s$ is the number of sites. For ferrite, the number of sites in the sub-lattices $s_1$ and $s_2$ are considered to be one and three, respectively, while in austenite, it is $a^{s_1} = a^{s_2} = 1$ [66]. The free energy of the pure and alloyed iron, $W_{Fe:Va}$ and $W_{Fe:C}$, respectively, along with the interaction parameter $\bar{L}_{Fe:Va,C}$, and the contribution from the magnetic ordering $W_m^{mo}$ are obtained from the CALPHAD database [67].

Considering the nature of Eqns. (25) and (26), both formulations of $W_{\mathrm{chem}}^\alpha$ can be approximated as

$$W_{\mathrm{chem}}^\alpha(c_i, c_j, T) = A^\alpha(T)c_i^2 + B^\alpha(T)c_j^2 + D^\alpha(T)c_i + E^\alpha(T)c_j + K^\alpha(T), \tag{27}$$

where $A^\alpha$, $B^\alpha$, $D^\alpha$, $E^\alpha$ and $K^\alpha$ are the coefficients that vary with temperature ($T$). Moreover, imposing the constraint $c_i + c_j = 1$, Eqn.

(22) transforms to

$$W^{\alpha}_{\text{chem}}(c_i, T) = O^{\alpha}(T)c_i^2 + P^{\alpha}(T)c_i + Q^{\alpha}(T), \tag{28}$$

where $O^{\alpha} = A^{\alpha} + B^{\alpha}$, $P^{\alpha} = D^{\alpha} - 2B^{\alpha} - E^{\alpha}$ and $Q^{\alpha} = B^{\alpha} + E^{\alpha} + K^{\alpha}$. To solve these coefficients, at a temperature $T$, the simplified free energy equation (Eqn. (28)) is differentiated, which yields

$$\frac{\partial^2 W^{\alpha}_{\text{chem}}}{\partial c_i^2} = 2O^{\alpha} = \frac{1}{\Omega}\cdot\frac{\partial^2 G^{\alpha}}{\partial c_i^2}, \tag{29}$$

$$\frac{\partial W^{\alpha}_{\text{chem}}}{\partial c_i} = 2O^{\alpha}c_i + P^{\alpha} = \frac{1}{\Omega}\cdot\frac{\partial G^{\alpha}}{\partial c_i} = \mu_i. \tag{30}$$

In the aforementioned equations, $\Omega$ denotes the molar volume of the individual phases, while $G^{\alpha}$ is the Gibbs free energy [67]. A coherent differentiation of the Gibbs free energy is achieved by a five-point stencil scheme in finite-difference approximation, which is expressed as

$$\frac{\partial^2 G^{\alpha}}{\partial c_i^2} = \frac{-G^{\alpha}_2 + 16G^{\alpha}_1 - 30G^{\alpha}_0 + 16G^{\alpha}_{\bar{1}} - G^{\alpha}_{\bar{2}}}{12(\Delta c_i)^2} \tag{31}$$

$$\frac{\partial G^{\alpha}}{\partial c_i} = \frac{-G^{\alpha}_2 + 8G^{\alpha}_1 - 8G^{\alpha}_{\bar{1}} + G^{\alpha}_{\bar{2}}}{12\Delta c_i}. \tag{32}$$

In the above equations, $G^{\alpha}_0$ corresponds to the Gibbs free energy at a given concentration $c_i^0$. To determine other free energy terms, a small concentration step $\Delta c_i$, which is generally less than $c_i^0$, is involved, such that $G^{\alpha}$ at $c_i^0 + \Delta c_i$, $c_i^0 + 2\Delta c_i$, $c_i^0 - \Delta c_i$ and $c_i^0 - 2\Delta c_i$ is expressed as $G^{\alpha}_1$, $G^{\alpha}_2$, $G^{\alpha}_{\bar{1}}$ and $G^{\alpha}_{\bar{2}}$, respectively. All free energy terms for a given combination of $c_i^0$ and $\Delta c_i$ can be obtained from the CALPHAD database. In the present work, the accuracy of the coefficients is further verified through a *Newton-Raphson iteration* technique by imposing the constraint $\partial G^{\gamma}_{eq}/\partial c = \partial G^{\alpha}_{eq}/\partial c$ at equilibrium (eq.), where $c$ is the carbon concentration [60]. The coefficients quantitatively defining the phases are tabulated in Table 1.

### 2.3. Comparison to existing models

The quantitative nature of the phase-field simulation, in addition to encompassing the physical conditions, is affirmed by the ability of the model to recover physical laws and sharp interface solutions. The equilibrium condition of a thermodynamical system with elastic and interfacial energy contribution is expressed as $[\![W_{\text{el}}]\!] - [\![\varepsilon]\!]\boldsymbol{n}\cdot\boldsymbol{\sigma}\boldsymbol{n} = -\gamma_{\alpha\beta}\kappa$. As elucidated in Ref. [68], the introduction of the chemical driving force modifies the equilibrium condition to

$$[\![W_{\text{chem}}]\!] - \sum_{i=1}^{K-1}\mu_i[\![c_i]\!] + [\![W_{\text{el}}]\!] - [\![\varepsilon]\!]\boldsymbol{n}\cdot\boldsymbol{\sigma}\boldsymbol{n} = -\gamma_{\alpha\beta}\kappa. \tag{33}$$

**Table 1**
Coefficients incorporating the CALPHAD data.

| Phase | Coefficients | Value |
|---|---|---|
| Ferrite | $O^{\alpha}$ | 4817708.33 |
| | $P^{\alpha}$ | 23828.12 |
| | $Q^{\alpha}$ | −40948.15 |
| Austenite | $O^{\gamma}$ | 147218.75 |
| | $P^{\gamma}$ | 20990.56 |
| | $Q^{\gamma}$ | −40692.69 |

Existing phase-field models [38,39], which are employed to simulate chemo-mechanical phase transformations like Widmanstätten structure, do not fulfill the equilibrium conditions. Furthermore, recently it has been identified that the approach adopting Voigt-Taylor homogenization scheme or Reuss-Sachs (RS) approximation render an inaccurate representation of the surface energy [63]. In the present model, the elastic driving force is formulated based on the jump conditions, which inherently leads to the mechanical configurational forces [63], and the chemical driving force is defined by the grand-potential functional [58]. This unique formulation of the driving force, under appropriate conditions as elucidated in Sec. 2.1, avoids the excess energy contribution to the interface by efficiently decoupling the bulk and interface contributions, and recovers the sharp interface solution [82]. The quantitative nature of the current approach is further enhanced by its ability to incorporate CALPHAD-based parameters [60]. As described in Sec. 2.2, since the parameters yield the equilibrium compositions identical to the database, the chemical driving force, which is dictated by the equi-partitioning of the diffusing component, is recovered for any given composition.

## 3. Simulation setup

### 3.1. Domain setup

The phase-field evolution equation (Eqn. (5)), which includes a variational derivative of the functional $\mathcal{F}$ (Eqn. (1)), along with the concentration (Eqn. (11)) and the chemical potential (Eqn. (12)) equations, is discretized on a uniform numerical grid using a finite-difference approach. These equations are solved with an explicit forward Euler scheme, and subsequently, the condition for the mechanical equilibrium $\nabla\cdot\overline{\boldsymbol{\sigma}} = 0$ is solved at every time step in a staggered manner. The present work considers a grid spacing of $\Delta x = \Delta y = 2.0 \times 10^{-9}$m, and all the simulations are performed in a two-dimensional domain of size 0.6 μm × 1.2 μm, resolved by 300 × 600 grid points along the x- and y-directions. The length scale parameter $\varepsilon$, which governs the width of the diffuse interface, is set to $\varepsilon = 2.5 \times \Delta x$, so that the interface comprises approximately 6 grid points. A zero-flux boundary condition is used for the phase-field and the concentration in all three directions. For the mechanical part a stress-free boundary condition is adopted along the x- and y-directions, while the displacements in the orthogonal directions of z are held at zero (Fig. 2a).

The proposed model is incorporated into the in-house software package PACE3D (Parallel Algorithms for Crystal Evolution in 3D) to enhance computational efficiency [69]. Moreover, the Message Passing Interface (MPI) standard which reduces the computation time by decomposing the larger domain into smaller fragments is employed to optimize the simulations. The accuracy of the simulations is further improved by non-dimensionalizing the input parameters using an appropriate scheme and subsequently introducing these dimensionless values. During the initialization, the condition for the mechanical equilibrium is established across the diffuse interface separating the phases.

### 3.2. Eigenstrain

The difference in the crystal structure between the parent and the evolving phase induces a strain during the phase transformation. Since this strain is introduced despite the absence of any external deformation (stress), it is referred to as stress-free transformation strain, or more generally as eigenstrain. In steels, the displacive martensite transformation involves the growth of a BCT-(Body Centered Tetragonal) structured phase in an austenite matrix of FCC (Face Centered Cubic) structure. The strain accompanying

this displacive transformation, which in the present study is the Bain strain, implies a definite orientation relation between the two constituent phases. Having established the close correspondence between the growth of Widmanstätten ferrite and martensite in the introduction (Sec. 1), an approach, adopted for the characterization of martensite in phase-field simulations [70], is extended for Widmanstätten ferrite. A schematic three-dimensional representation of this Bain strain in relation to the crystal structure of the phases is presented in Fig. 1a.

The definite orientation relation between the FCC austenite ($\gamma$) and the BCC (Body Centered Cubic) ferrite ($\alpha$) accompanying the Bain strain can be expressed as

$$[101]_\gamma \,||\, [100]_\alpha \quad [010]_\gamma \,||\, [010]_\alpha \quad \left[\bar{1}01\right]_\gamma \,||\, [001]_\alpha. \tag{34}$$

In 3D, this crystallographic relation between the phases yields three distinct variants of Bain strain. However, since the phase transformation in the present study is confined to 2D, a simplified Bain strain which yields two variants, as shown in Fig. 1b, is considered. These two variants of the Bain strain are expressed as

$$\tilde{\boldsymbol{\varepsilon}}^{00}(1) = \begin{pmatrix} \varepsilon_3 & 0 & 0 \\ 0 & \varepsilon_1 & 0 \\ 0 & 0 & 0 \end{pmatrix}, \quad \tilde{\boldsymbol{\varepsilon}}^{00}(2) = \begin{pmatrix} \varepsilon_1 & 0 & 0 \\ 0 & \varepsilon_3 & 0 \\ 0 & 0 & 0 \end{pmatrix}. \tag{35}$$

The stress-free transformation strains $\varepsilon_1$ and $\varepsilon_3$ are calculated through the relations $\varepsilon_1 = (\sqrt{2}\,a_\alpha - a_\gamma)/a_\gamma$ and $\varepsilon_3 = (c_\alpha - a_\gamma)a_\gamma$, where $a_\alpha$, $c_\alpha$ and $a_\gamma$ are the lattice parameters of ferrite and austenite, respectively [72]. Here, it is important to note that this Bain strain exclusively accounts for the elastic strain which is induced during the phase transformation. However, often these displacive transformations accompany plastic relaxation, characterized by an increase in dislocation density, which reduces the elastic strain [21–24]. Furthermore, using the phase-field approach, the plastic relaxation accompanying the diffusion-controlled evolution of Widmanstätten plates has been analyzed recently [51]. Accordingly, chemo- and thermo-elastic models adopted respectively for the simulation of bainite and martensite, reduce the eigenstrains appropriately to account for the plastic relaxation [63,73]. The crystallographic analysis of Widmanstätten ferrite suggests an approximate shear strain of 0.36, and a dilatational strain of 0.03 [19]. The influence of the plastic relaxation, which is observed during the growth of the Widmanstätten plate, is incorporated by reducing the shear strain to 0.12, while approximately retaining the dilatational strain. This reduction in the eigenstrain is achieved by the values of $\varepsilon_1 = 0.08$ and $\varepsilon_3 = -0.04$.

### 3.3. Setup optimization

It is well established that boundary conditions have a considerable influence on the simulation results. Setting-up an enormously large domain to reduce these impacts is computationally ill-favored. Thus alternatively, the contribution from the domain boundaries is efficiently minimized by pre-defining the growth direction of the inclusion (nucleus). In order to achieve growth in the desired direction, in the present work, the eigenstrain tensor $\tilde{\varepsilon}^{00}_{ij}$ is initially rotated using the rotation matrix $Q$, according to the $z - y' - x''$ intrinsic rotation convention which yields $\tilde{\varepsilon}^{0}_{ij}$, expressed as $\tilde{\varepsilon}^{0}_{ij} = Q_{im}Q_{jn}\tilde{\varepsilon}^{00}_{mn}$. Furthermore, to ascertain the degree of rotation which is required to facilitate the growth in the direction of minimal boundary influence, a function $B(n)$, expressed as

$$B(n) = \mathscr{C}_{ijkl}\tilde{\varepsilon}^{0}_{ij}\tilde{\varepsilon}^{0}_{kl} - n_i\sigma^{0}_{ij}\Omega_{jl}(n)\sigma^{0}_{lm}n_m \tag{36}$$

is involved, where $\sigma^{0}_{ij} = \mathscr{C}_{ijkl}\tilde{\varepsilon}^{0}_{kl}$, and the inverse Green function tensor reads $(\boldsymbol{\Omega}^{-1}(n))_{ij} = \mathscr{C}_{iklj}n_k n_l$, with $n$ representing the vector normal to the broad-faces of the acicular inclusion [74]. The function $B(n)$, which relates the eigenstrain to the elastic energy, facilitates the depiction of this relation as polar plots. This polar plot for the aforementioned eigenstrain is shown in Fig. 2a. The anisotropy in the elastic energy, which governs the morphology of the evolving phase, is evident from this representation. Furthermore, the elastic-energy polar plot reveals that in the present unrotated condition, the normal of the broad-faces $n$ deviates from the crystallographic axis $[100]_\alpha$ (x-axis) by a degree of $\theta = -54.7^\circ$. Therefore, a counter-acting rotation of $\theta = 54.7^\circ$ is imposed to align $n$ along the $[100]_\alpha$-axis, so that the growth of the nucleus along the desired $[010]_\alpha$ axis (y-axis) is established. In Fig. 2b, the elastic energy plot after the rotation, which minimizes the influence of the domain boundaries by fixing the growth direction, is shown. Since a comprehensive elucidation of the elastic energy plots and its implication is beyond the scope of the present work, readers are directed to Refs. [38,74] for further understanding.

## 4. Result and discussion

### 4.1. Dominance of elasticity over chemical driving force

By introducing the aforementioned elastic parameters $\varepsilon_1$ and $\varepsilon_3$, a Bain variant representing the Widmanstätten ferrite nucleus is allowed to evolve. The chemical, elastic and interfacial parameters governing this evolution are presented in Tables 2 and 3, respectively. Isotropic elastic moduli for cubic crystals are used for both the austenitic as well as the ferritic phase, which are calculated based on Young's modulus $E$ and Poisson's ratio $\nu$. The temperature

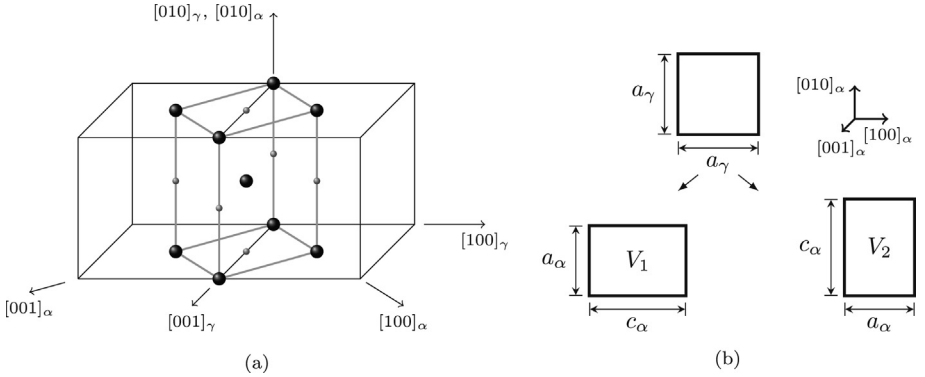


**Fig. 1.** Bain correspondence. a) Formation of a BCT phase [71]. The positions of iron atoms are marked with large spheres, possible positions of carbon atoms are marked with small spheres. Not all atoms are displayed. b) In 2D, two Bain variants originate from the austenitic phase.

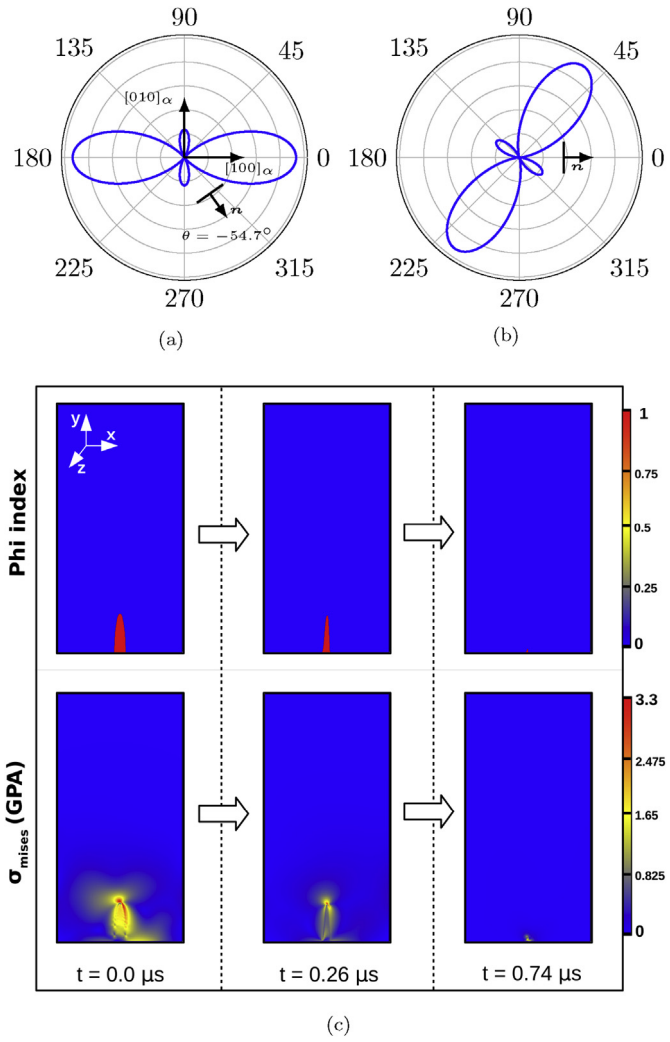


**Fig. 2.** a) and b) The elastic anisotropy introduced by the eigenstrains is presented as plots. (a) In an unrotated condition, the growth direction determined through $n$ deviates significantly from the desired direction. (b) A rotation is imposed to enable the growth along the direction where the influence of the boundary condition is minimal. c) Temporal evolution of the ferrite nucleus. Owing the lack of sufficient chemical driving force, the nucleus shrinks failing to overcome the mechanical barrier.

of 980 K and the overall composition of 0.4 wt.% carbon is chosen to relate directly to experimental observation which has been reported earlier [46]. The temporal evolution of the Widmanstätten ferrite, under these condition, is illustrated in Fig. 2c. Consistent with the theoretical indications [45,46], despite the reduced eigenstrains and the preferred growth direction, it is evident that the ferrite nucleus fails to grow and ultimately disappears at high temperatures. This behavior indicates that the chemical driving force is inadequate to overcome the strain induced by the phase transformation, and thus leads to the shrinkage of the ferrite nucleus.

**Table 2**
CALPHAD-based parameters governing the evolution of the Widmanstätten ferrite at 980 K.

| Parameter | Value |
|---|---|
| Temperature $T$ | 980 K |
| Diffusivity in ferrite $D_\alpha$ | $2 \times 10^{-9}$ $m^2s^{-1}$ |
| Diffusivity in austenite $D_\gamma$ | $1 \times 10^{-9}$ $m^2s^{-1}$ |
| Overall carbon concentration $c$ | 0.01805 mol frac. (0.4 wt.%) |
| Ferrite eq. concentration $c^\alpha_{eq}$ | 0.000973 mol frac. (0.021 wt.%) |
| Austenite eq. concentration $c^\gamma_{eq}$ | 0.041 mol frac. (0.91 wt.%) |

**Table 3**
Elastic and interfacial parameters.

| Parameter | Value |
|---|---|
| Interfacial energy $\gamma_{\alpha\beta}$ | 0.2 $J/m^2$ [38] |
| Third order parameter $\gamma_{\alpha\beta\delta}$ | $15\gamma_{\alpha\beta}$ $J/m^2$ |
| Young's modulus $E$ | 130 GPa [39] |
| Poisson's ratio $\nu$ | 0.33 [39] |

### 4.2. Co-operative growth of 'back-to-back' plates

#### 4.2.1. Transformation mechanism

As discussed in Sec. 1, based on experimental observations [46,49,50], it is postulated that the Widmanstätten ferrite grows as self-accommodating plates at high temperatures, close to Widmanstätten start-temperature ($W_s$),. This back-to-back co-operative growth of plates compensates the low chemical driving force by mutually eliminating the shear component of the strain. In 2D, the two variants of Bain strain, illustrated in Fig. 1b, are potentially capable of mutually annulling the shear strain. Therefore, both these variants are considered to simulate the self-accommodating growth of Widmanstätten ferrite plates. As elucidated in Sec. 4.1, prior to the simulation, the variants are appropriately rotated to achieve co-operative growth of plates along the desired $[010]_\alpha$ crystallographic axis. The unrotated and rotated elastic energy plots of both variants are presented in Fig. 3a and b, respectively.

Furthermore, the simulation domain is constructed in such a way that the nuclei of the plates exhibit a back-to-back relation.

The temporal evolution of the plate nuclei begins with an initialization stage during which the inclusions adapt to the imposed eigenstrain. In the subset of Fig. 3c, the ferrite nuclei at $t = 0$, prior to the initialization, are shown. This initialization is subsequently followed by the co-operative growth of the plates as shown in Fig. 3c. In complete agreement with the displacive theory, despite the lack of sufficient chemical driving force to facilitate the growth of a single plate, by the co-operative growth of self-accommodating plates, the Widmanstätten structure is obtained using the present phase-field model. Furthermore, it is evident from the graphical representation (Fig. 3c) that the curvature at the tip of the Widmanstätten structure, which encompasses both variants, remains noticeably unchanged through the entire evolution. Similar energetically favored back-to-back growth of bicrystals has been reported earlier [75], however, the crystallographic consideration and the chemical driving force involved in the transformation differ significantly.

The change in the distribution of carbon concentration, accompanying the growth of the Widmanstätten ferrite, is included in Fig. 3c. In adherence to the Gibbs-Thomson relation, the carbon concentration at the tip of the plate varies substantially from the concentration around the broad-faces, owing to the inherent difference in the curvature. Although the evolution of the Widmanstätten structure involves the self-accommodating growth of two plates, its influence on the carbon distribution is imperceptible. This theoretically consistent behavior, exhibited by the carbon concentration in resembling the distribution, which is typically associated with the growth of the single plate, ensures that the kinetics of the transformation complies with the thermodynamical predictions. Thus, in addition to the eigenstrain, the low concentration at the tip favors the growth of the ferrite along the $[010]_\alpha$-axis, ultimately resulting in the Widmanstätten

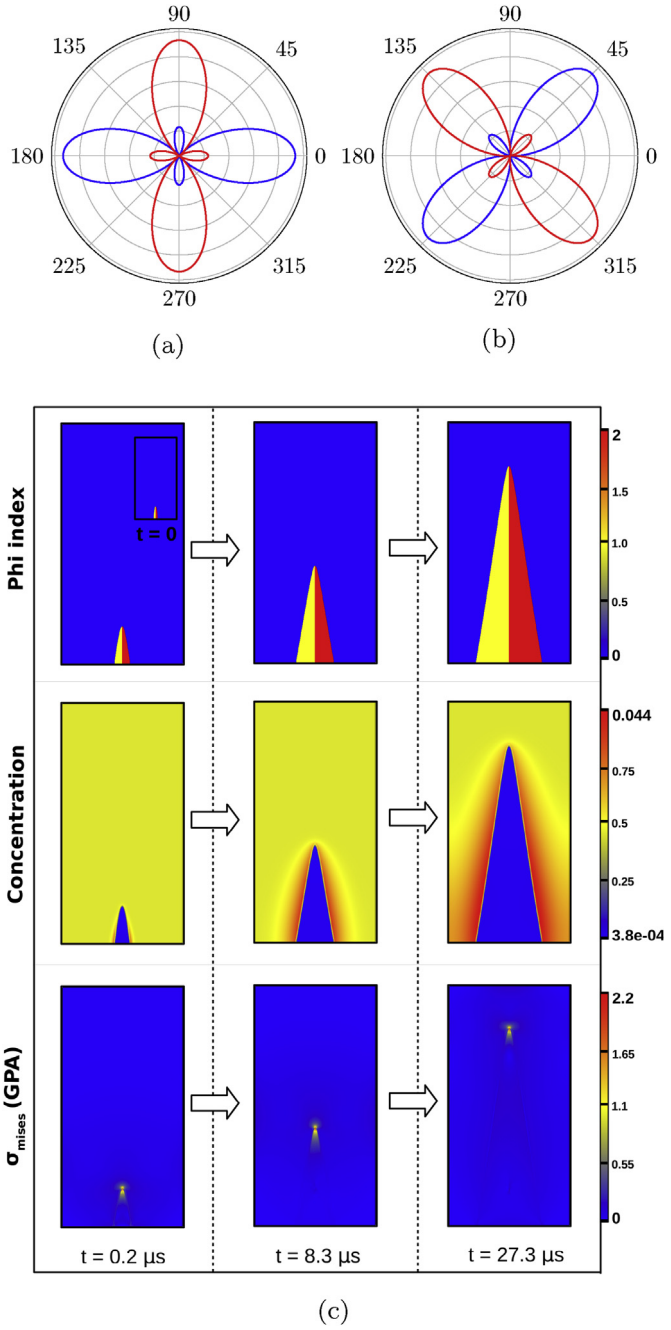


**Fig. 3.** a) and b) The polar plot representing the anisotropic elastic energy of both variants of Bain strain in an unrotated and rotated condition. c) The ferrite nuclei, introduced into the domain as back-to-back acicular structure, are shown in the subset. The growth of these mutually-accommodating ferrite plates, after the initialization, is achieved by canceling out the shear strain $\sigma_{\text{mises}}$ along the broad-faces. The evolution of the carbon concentration resembles the growth of a single Widmanstätten structure.

morphology. In order to monitor the elastic component of the transformation, the von Mises stress is calculated during the growth of the Widmanstätten ferrite, which is illustrated in Fig. 3c. It is evident that the von Mises stress, during the transformation, is extensively confined to the tip of the plates and is significantly absent along the broad-faces. The self-accommodating nature of the plates, which is characterized by the counterbalancing of the shear strains, is indicated by this lack of $\sigma_{\text{mises}}$ along the $[100]_\alpha$-axis. In addition to the anisotropy in the elastic energy, this neutralization of the shear strains cumulatively governs the morphology exhibited by the growing phase.

The concentration evolution accompanying the back-to-back co-operative growth of plates, illustrated in Fig. 3c, indicates that, kinetically, this transformation can be treated as the growth of a single plate. Thus, in order to substantiate this claim, the growth kinetics of the self-accommodating transformation is analyzed with respect to the existing analytical predictions for the single plate.

#### 4.2.2. Transformation kinetics

In a Widmanstätten structure, the broad-faces are often distinguished from the curved tip. The influence of the curvature on the evolution of the broad-faces, which are almost flat, is negligible when compared to the tip. Furthermore, as shown in Fig. 3c, the shear stress around these broad-faces is noticeably absent. Thus, in a carbon-diffusion governed transformation, the lateral growth of the Widmanstätten ferrite is considered to follow the parabolic law [76]. In other words, the position of the broad-face $x$ is related to the time $t$ through the relation $x \propto \sqrt{t}$. The position of the interface along the crystallographic axis $[100]_\alpha$ during the growth of the Widmanstätten ferrite is monitored and plotted against time in Fig. 4a. Owing to the diffuse nature of the interface, an isoline representation wherein $\phi_\alpha = 0.5$ is considered to track the interface in Fig. 4a and all the similar plots. Fitted data-points, in this illustration, unravel the thermodynamical consistency of the present simulation by capturing the lateral growth of the Widmanstätten structure. Here, it is worth mentioning that $x_t$, the position of the interface at time $t$, is normalized with its initial position $x_0$, for the broad-faces and the tip, to provide a cumulative representation of the growth kinetics. Unlike the broad-faces, the curvature at the tip of the plate significantly influences its migration during the transformation. The concentration at the migrating interface of the tip deviates from the local-equilibrium condition, or para-equilibrium condition in ternary system, in accordance with the radius of the curvature [76]. Thus, any change in the radius of the tip during the evolution, correspondingly changes the concentration ahead of the plate, which subsequently introduces a change in the growth kinetics. However, experimentally, it has been identified that the Widmanstätten plate lengthens at a constant rate [10]. This time-independent transformation kinetics of the plate implies a constant chemical driving force along the growth direction, which imposes a constraint on the tip curvature. It has been established in Sec. 2.3 that, despite the diffuse interface, the jump condition involved in the formulation of the present phase-field model recovers the sharp-interface consideration. In addition to this claim, in order to ensure that the curvature introduced by the eigenstrains at the tip of the plate is preserved during the evolution, the position of the tip is investigated. A constant growth rate of the plate indicates that the migration of the tip, as opposed to the broad-faces, follows a linear growth law, which translates into a relation $x \propto t$, where $x$ is the position of the tip and $t$ is the time. The temporal change in the position of the tip, shown in Fig. 4b, complies entirely with the predicted linear growth law, thereby indicating the curvature-preservation at the tip during the growth of the Widmanstätten structure. Collectively, for the first time, the present analysis renders a thermodynamically-consistent theoretical support to the co-operative growth of self-accommodating Widmanstätten ferrite plates through a chemo-elastic phase-field model.

#### 4.2.3. Triple junction in 'back-to-back' plates

Unlike the conventional Widmanstätten structure, a triple junction is introduced at the tip of the self-accommodating plates. The shape of this triple junction is monitored during the growth of

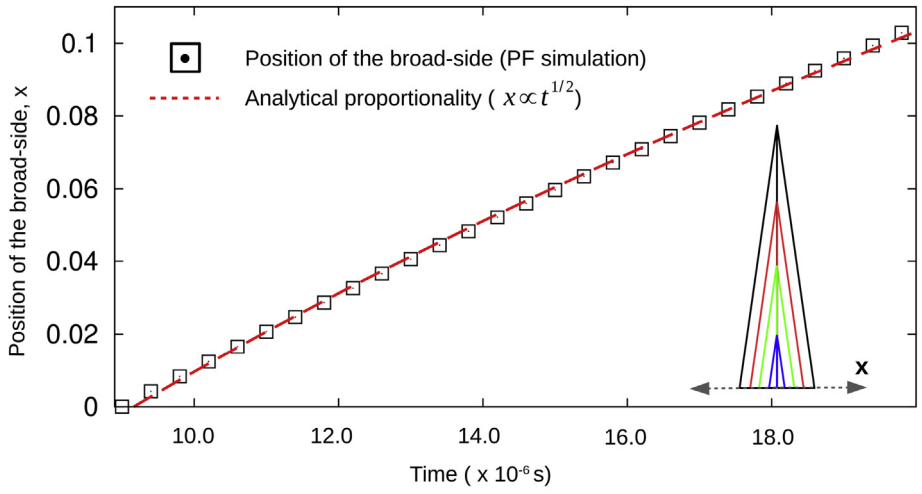


(a)

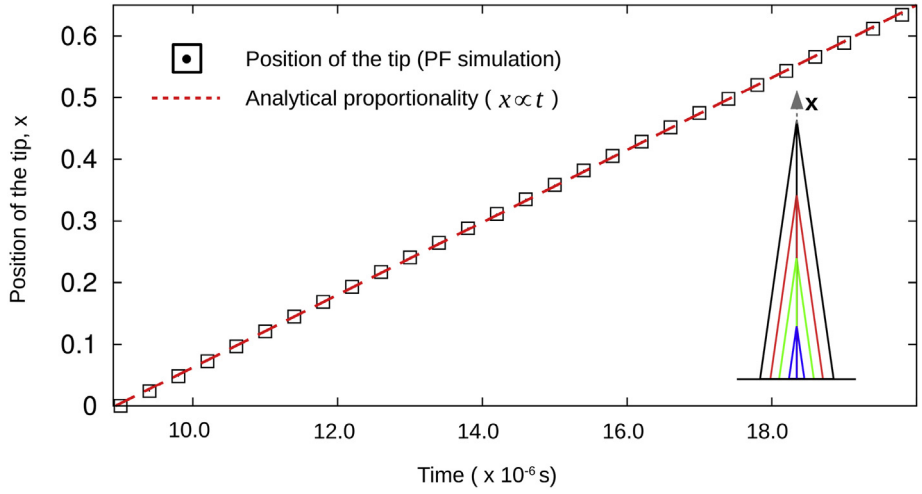


(b)

**Fig. 4.** (a) The growth kinetics of the broad-faces of the Widmanstätten ferrite wherein the influence of the curvature is negligible. b) The migration of the interface at the tip of the ferrite structure is monitored and plotted against time. Since two distinct plates are involved in this Widmanstätten structure, the interface pertaining to the austenite is considered ($\phi^{\gamma} = 0.5$).

the plates and the profile of the tip is illustrated in Fig. 5. Consistent with the kinetics of the evolution, as presented in the previous section, the morphology of the tip remains unaltered throughout the transformation. The characteristic profile of the tip is predominantly dictated by two factors; the interfacial energy between the phases and the eigenstrain. Therefore, a complete adherence to the young's law cannot be expected.

In the current analysis, the interfacial energy between the two variants $\alpha_1$ and $\alpha_2$ is considered to be equal to the interfacial energy between the parent and the evolving phase ($\gamma_{\alpha_1\gamma} = \gamma_{\alpha_2\gamma} = \gamma_{\alpha_1\alpha_2}$). Furthermore, the eigenstrains are calculated based on the experimental observation [19]. The combination of these parameters yields the profile observed in Fig. 5. It is conceivable that any change in either the interfacial energy or the eigenstrain would alter the shape of the triple junction. This change in the profile would consequently affect the kinetics of the evolution. However, as shown in Fig. 4b, for the parameters considered in the present study, no significant deviation is introduced in the kinetics of the phase transformation.

It is conceded that, in the phase-field modelling, the interface width influences the curvature at the tip. However, it should be realized that unlike phase-field simulation wherein high anisotropic strength is introduced to achieve the Widmanstätten morphology [35–37,40], the present work employs elastic strain. Therefore, the influence of the anisotropy on the interface width is largely averted [41]. Furthermore, as discussed in Sec. 2.3, in the present model, the driving forces are specifically formulated to avoid any such influence on the interface. Consequently, and since profile of the tip are predominantly governed factors like the interfacial energy and the eigenstrain, it is reasonable to assume that any deviation introduced by interface width do not significantly influence the kinetics of the transformation. Nevertheless, this unphysical aspect of the simulation are extensively investigated to quantify the inaccuracy introduced by the interface width, which will be reported in the upcoming works.

### 4.3. Growth of a single Widmanstätten ferrite plate

#### 4.3.1. Transformation mechanism

With decrease in temperature, the chemical driving force

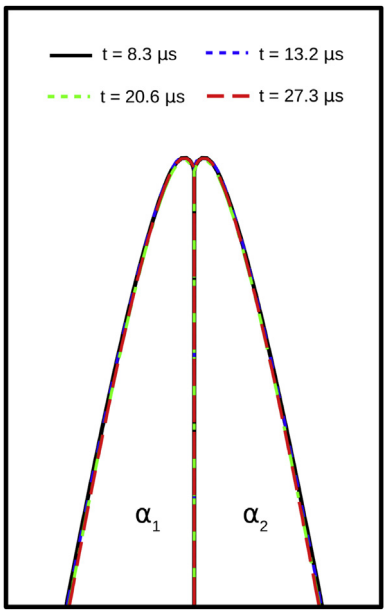


**Fig. 5.** An isoline representation ($\phi_{\alpha_1} = \phi_{\alpha_2} = 0.5$) of the triple junction formed at the tip of the mutually-accommodating plates during its evolution.

governing the transformation increases sufficiently to overcome the mechanical barrier introduced by the eigenstrains. This increase in the driving force enables the growth of a single plate (Bain variant), despite the change in the strains associated with the change in the temperature. In this section, the temporal evolution of a single ferrite plate at 873 K is analyzed. The parameters governing the chemical driving force in this simulation are presented in Table 4.

While the equilibrium concentrations of the constituent phases, ferrite and austenite, are changed in accordance with the CALPHAD database, the diffusivities in each of the phases are retained assuming no significant change. Furthermore, the overall composition of the system is chosen to ensure that the chemical driving force, through the supersaturation, remains comparable in both simulations. In order to accommodate the change in the stored energy introduced by the decrease in the transformation temperature [77], the engineering shear strain is increased to 0.16 through the eigenstrains of $\varepsilon_1 = 0.08$ and $\varepsilon_3 = -0.08$. Furthermore, similar to the existing phase-field study the dilatational strain is overlooked for the simulation of the single Widmanstätten plate [39].

The anisotropy in the elastic energy of a single Bain variant, with the increased shear strain, is shown in Fig. 6a. The rotated polar plot which ensures the growth of the plate in the desired crystallographic axis is included. Fig. 6c presents the growth of a single ferrite plate at 873 K. Similar to the transformation at 980 K, in the initial stages of the transformation, the tip of the plate adapts a curvature much different from the nucleus, but dependent on the imposed eigenstrain. However, after the initialization, this curvature remains visibly unaltered throughout the simulation. Furthermore, consistent with experimental observations [46,49,78], the aspect ratio of the plate significantly differs from the previous simulation (980 K). Despite the increase in the strain, a relatively high aspect ratio, ratio of the height to the width of the plate, is observed at low temperature (873 K). The evolution of the concentration distribution, in accordance with the difference in the curvature between the flat broad-faces and the tip of the plate, is illustrated in Fig. 6c. Moreover, the temporal change in the von Mises stress accompanying the transformation is included as well.

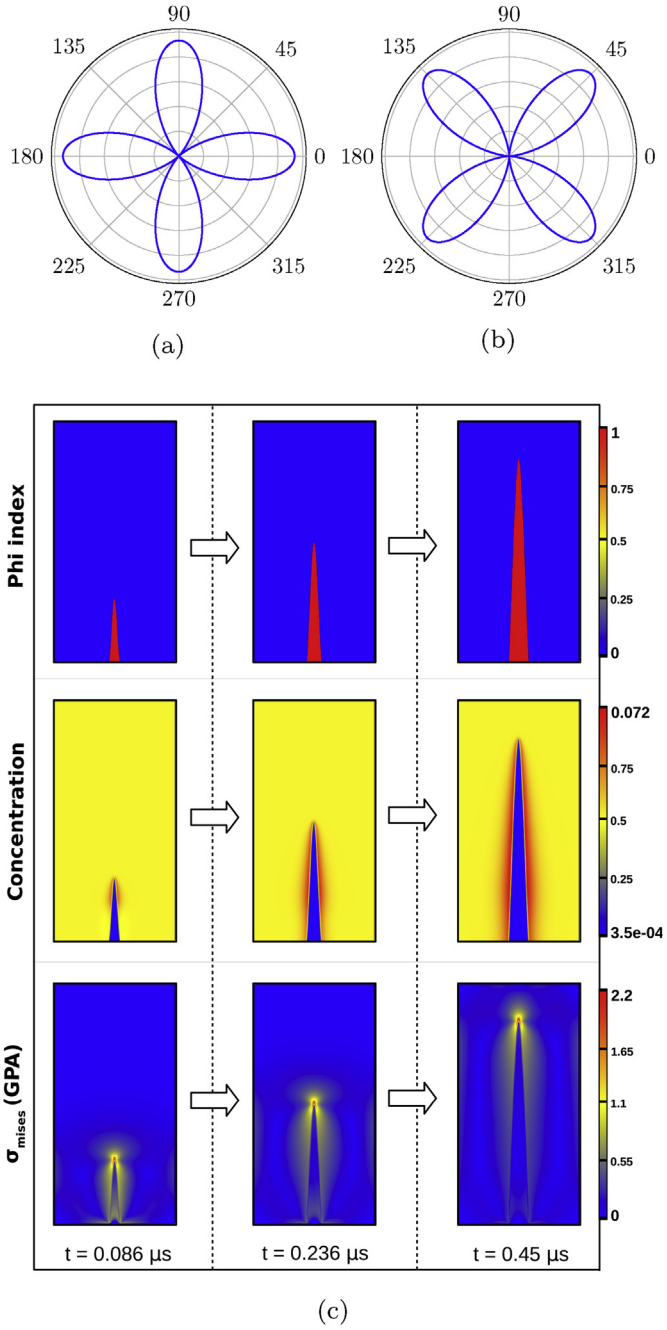


**Fig. 6.** a) and b) Rotated and unrotated representation of the elastic energy of a singly Bain variant, respectively. c) Growth of a single Widmanstätten plate at low temperature, wherein the chemical driving force is high enough to overcome the mechanical barrier imposed by the eigenstrains.

**Table 4**
CALPHAD-based parameters governing the evolution of the Widmanstätten ferrite at 873 K.

| Parameter | Value |
|---|---|
| Temperature $T$ | 873 K |
| Diffusivity in ferrite $D_\alpha$ | $2 \times 10^{-9}$ $m^2s^{-1}$ |
| Diffusivity in austenite $D_\gamma$ | $1 \times 10^{-9}$ $m^2s^{-1}$ |
| Overall carbon concentration $c$ | 0.036 mol frac. (0.8 wt.%) |
| Ferrite eq. concentration $c^{\alpha}_{eq}$ | 0.0013 mol frac. (0.02 wt.%) |
| Austenite eq. concentration $c^{\gamma}_{eq}$ | 0.081 mol frac. (1.8 wt.%) |

Owing to the anisotropy in the elastic energy, the stress at the tip is significantly high when compared to the broad-faces. Here, it is interesting to note that, although a slight traces of von Mises stress is noticed in the broad-faces during the growth of the single plate, these stresses are relatively absent in the back-to-back growth of plate shown in Fig. 3c. This lack of von Mises stress in the broad-faces of the mutually-accommodating plates further vindicates the canceling out of the shear component of the stress.

*4.3.2. Transformation kinetics*

The growth kinetics of the Widmanstätten plate is analyzed by tracking the temporal migration of the tip and broad-faces, separately. Similar to the co-operative growth of the self-accommodating plates, the tip, governed by the curvature, exhibits a time-independent growth rate, characterized by the relation $x \propto t$ as shown in Fig. 7a, where $x$ and $t$ represent the position of the tip and time, respectively. Furthermore, Fig. 7b indicates that the lateral growth of the Widmanstätten ferrite holds a parabolic relation with time $t$, which is expressed as $x \propto \sqrt{t}$, owing to its almost flat surface.

Although the present investigations primarily focus on the evolution of the Widmanstätten structure governed by the eigenstrains, the role of the chemical driving force cannot be entirely overlooked. Therefore, to understand the influence of the chemical driving force on the transformation kinetics, the growth of the Widmanstätten plate is analyzed under different supersaturations for the given eigenstrains. The supersaturation is varied by changing the overall concentration of the system ($c^{\gamma}_{\infty}$). Correspondingly, the chemical driving force is quantified as $\tilde{\Omega} = (c^{\gamma}_{eq} - c^{\gamma}_{\infty})/(c^{\gamma}_{eq} - c^{\alpha}_{eq})$. The influence of the supersaturation on the kinetics of the evolution is expressed by the Ivantsov's relation [79], $\tilde{\Omega} = \sqrt{\pi P}\exp(P)\mathrm{erfc}(\sqrt{P})$, where the Péclet number $P = (V_{pl}R_{pl})/(2D_{\gamma})$ depicts the normalized velocity with $R_{pl}$, $D_{\gamma}$ and $V_{pl}$ representing the radius of the Ivantsov's parabola, diffusivity and the growth velocity, respectively. The change introduced in the transformation kinetics by the different supersaturations is determined by monitoring the migration velocity ($V_{pl}$) and is plotted in Fig. 8. The visible deviation from the curve is expected since the theoretical model does not consider elasticity. However, despite the deviation, it is noticeable that the role of the supersaturation in influencing the

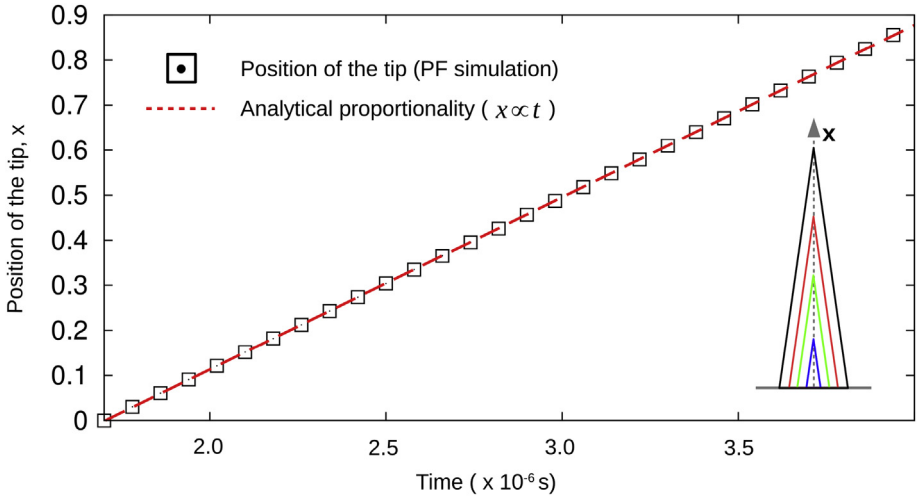


(a)

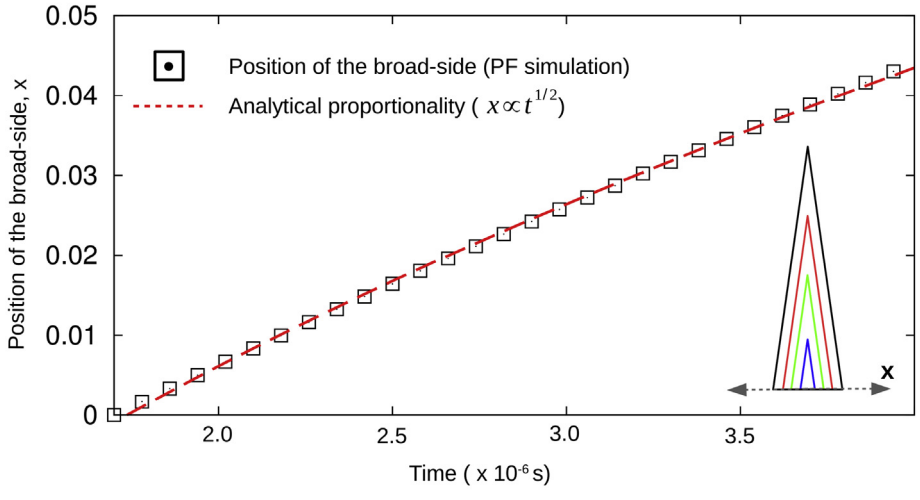


(b)

**Fig. 7.** (a) The migration of the tip, owing to the influence of the curvature on the concentration distribution, adheres to the relation $x \propto t$. b) The lateral growth of the Widmanstätten ferrite follows the parabolic relation $x \propto \sqrt{t}$.

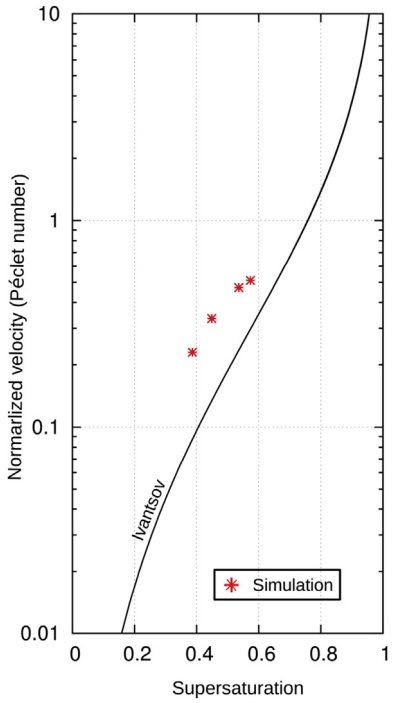


**Fig. 8.** Influence of the supersaturation on the kinetics of the evolution is compared with the Ivantsov's prediction [79].

transformation kinetics follows an apparently similar trend to the Ivantsov's model. This systematic shift is attributed to the consistent interplay of the chemical and the elastic contributions [80].

## 5. Summary

Properties of any given material significantly depend on the phases that constitute its microstructure. In addition to the chemical composition and the crystal structure of the phase, the morphology it adopts during the transformation plays a pivotal role in influencing the material properties. One of such structurally distinct phase transformations in steels, which considerably affects the mechanical properties, is the growth of Widmanstätten ferrite. Despite the extensive application and research on steels, certain aspects of this transformation are still under contention. Although the present study does not provide or intends to provide a definitive solution to this contention, yet different from the most phase-field studies [35–37,40], a thermodynamically-consistent chemo-elastic model is employed to simulate the growth of the Widmanstätten structure under different chemical driving forces. The displacive theory on the growth of Widmanstätten ferrite suggests that at high temperatures, wherein the chemical driving force is not high enough to overcome the mechanical barrier imposed by the eigenstrain, the plates grow in a co-operative self-accommodating manner. This accommodating growth of the plates reduces the mechanical barrier by mutually neutralizing the shear component of the strain. While the carbon-diffusion governed back-to-back growth of the Widmanstätten-ferrite plates has been observed experimentally [46,49,50], simulation studies based on the displacive theory overlook this aspect of the transformation [38,39]. Thus, the present work begins with the formulation of a chemo-elastic phase-field model by adopting a specific jump condition, which retains the sharp-interface solutions despite the involvement of the diffuse interface. Furthermore, the formulation allows the incorporation of CALPHAD-based parameters which render quantitative chemical driving force, governed by the transformation temperature and supersaturation.

By employing the formulated multicomponent multiphase-field model, it is shown that the regular growth of the Widmanstätten structure is not favored at high temperatures, owing to the lack of sufficient chemical driving force. However, by involving both variants of the Bain strain (in 2D), under a similar chemical environment, the Widmanstätten structure is achieved by the mutually-accommodating growth of the plates. Despite the difference in the transformation mechanism and the involvement of two different plates, no significant distinction is identified in the temporal evolution of the carbon concentration. While this observation affirms the consistency in the chemical driving force governed by the equi-partitioning of carbon, the neutralization of the shear strain is captured by monitoring the von Mises stress during the transformation.

The growth of a single Widmanstätten ferrite plate is simulated by reducing the transformation temperature and by appropriately changing the CALPHAD-based parameters. Consistent with the experimental observation, at low temperatures, the chemical driving force overcomes the mechanical barrier, and thus enables the growth of a single ferrite plate [46]. The growth kinetics of the plates, under different conditions, are analyzed separately to verify the consistency of the transformation with the analytical predictions. In complete agreement with the thermodynamical predictions [76], under both transformation temperatures, it is shown that the migration of the tip adheres to the linear growth law, while the broad-faces follow the parabolic growth law. In the present work, it is conceded that the specific choice of eigenstrains, after compensating for the plastic relaxation, in both transformations is not entirely quantitative. However, given the lack of a complete understanding on the influence of the plastic relaxation, reasonable assumptions of these eigenstrains are made. Motivated by Ref. [81], attempts are being made, which will be reported in the future, wherein plasticity is included in a similar phase-field formulation to quantify the plastic relaxation at different temperatures. Furthermore, simulations of chemo-mechanical phase transformations involving other orientation relations with increased number of variants will be pursued.

## Acknowledgments

First impetus was given within the research activities of the Graduate School - 1483 funded by the German Research Foundation (DFG) which we greatly appreciate. The authors acknowledge the financial support of Ministry of Science, Research and Arts of Baden-Wuerttemberg under the grant 33-7533.-30-10/25/54. The authors are also grateful for the editorial support by Leon Geisen and the assistance with mathematical questions by Oleg Tschukin. This work was performed on the computational resource ForHLR II, funded by the Ministry of Science, Research and Arts of Baden-Wuerttemberg and the DFG.

## References

[1] G.Z. Koval'chuk, V.N. Geichenko, V.N. Yarmosh, L.V. Podobedova, Effect of widmanstatten ferrite on some properties of hypoeutectoid steel, Met. Sci. Heat Treat. 21 (2) (1979) 114–117.
[2] J.N. Cordea, Symp. On Low Alloy High Strength Steels, 1970.
[3] R.L. Bodnar, S.S. Hansen, Effects of widmanstätten ferrite on the mechanical properties of a 0.2 pct c-0.7 pct mn steel, Metall. Mater. Trans. A 25 (4) (1994) 763–773.
[4] John M. Chilton, M.J. Roberts, Microalloying effects in hot-rolled low-carbon steels finished at high temperatures, Metall. Mater. Trans. A 11 (10) (1980) 1711–1721.
[5] V. Muthupandi, P Bala Srinivasan, S.K. Seshadri, S. Sundaresan, Effect of weld metal chemistry and heat input on the structure and properties of duplex stainless steel welds, Mater. Sci. Eng. A 358 (1) (2003) 9–16.

[6] Clarence Zener, Kinetics of the decomposition of austenite, Trans. Aime 167 (1946) (1946) 550–595.
[7] J.W. Cahn, W.C. Hagel, Decomposition of Austenite by Diffusional Processes, vol. 131, Interscience, New York, 1962.
[8] M.G. Hall, H.I. Aaronson, K.R. Kinsma, The structure of nearly coherent fcc: bcc boundaries in a cu-cr alloy, Surf. Sci. 31 (1972) 257–274.
[9] K.C. Russell, M.G. Hall, K.R. Kinsman, H.I. Aaronson, The nature of the barrier to growth at partially coherent fcc: bcc boundaries, Metall. Mater. Trans. B 5 (6) (1974) 1503–1505.
[10] E.P. Simonen, H.I. Aaronson, R. Trivedi, Lengthening kinetics of ferrite and bainite sideplates, Metall. Trans. 4 (5) (1973) 1239–1245.
[11] R. Trivedi, G.M. Pound, Growth kinetics of plate-like precipitates, J. Appl. Phys. 40 (11) (1969) 4293–4300.
[12] R. Trivedi, The role of interfacial free energy and interface kinetics during the growth of precipitate plates and needles, Metall. Mater. Trans. B 1 (4) (1970) 921–927.
[13] J.M. Rigsbee, H.I. Aaronson, The interfacial structure of the broad faces of ferrite plates, Acta Metall. 27 (3) (1979) 365–376.
[14] Masato Enomoto, Thermodynamics and kinetics of the formation of widmanstätten ferrite plates in ferrous alloys, Metall. Mater. Trans. A 25 (9) (1994) 1947–1955.
[15] N.T. Belaiew, The inner structure of the crystal grain as revealed by meteorites and widmanstiitten figures, J. Inst. Met. 29 (1923) 379–406.
[16] Y.C. Liu, H.I. Aaronson, K.R. Kinsman, M.G. Hall, The habit plane of widmanstätten ferrite sideplates, Metall. Trans. 3 (5) (1972) 1318–1320.
[17] B.A. Bilby, J.W. Christian, The crystallography of martensitic transformations, J. Iron Steel Inst. 197 (1961) 122–131.
[18] J.W. Christian, Martensitic Transformations-a Current Assessment, 1969.
[19] J.D. Watson, P.G. McDougall, The crystallography of widmanstätten ferrite, Acta Metall. 21 (7) (1973) 961–973.
[20] J.M. Prado, J.J. Catalan, M. Marsal, Dilatometric study of isothermal phase transformation in a c-mn steel, J. Mater. Sci. 25 (4) (1990) 1939–1946.
[21] Yasuya Ohmori, Hiroyuki Ohtsubo, ichiro Georgima Ken, Nobuaki Maruyama, Growth of bainite and widmanstätten ferrite, Mater. Trans., JIM 34 (3) (1993) 216–223.
[22] Yasuya Ohmori, Hiroyuki Ohtsubo, Yun Chul Jung, Shuji Okaguchi, Hiroo Ohtani, Morphology of bainite and widmanstätten ferrite, Metall. Mater. Trans. A 25 (9) (1994) 1981–1989.
[23] Yasuya Ohmori, Yun-Chul Jung, Hiroaki Ueno, Kiyomichi Nakai, Hiroyuki Ohtsubo, Crystallographic analysis of upper bainite in fe-9% ni–c alloys, Mater. Trans., JIM 37 (11) (1996) 1665–1671.
[24] Yun-Chul Jung, Sung-Joon Kim, Yasuya Ohmori, Morphology and growth process of bainitic ferrite in steels, Met. Mater. Int. 4 (2) (1998) 125–134.
[25] E.S. Machlin, Morris Cohen, Burst phenomenon in the martensitic transformation, Trans. Metall. Soc. AIME 191 (1951) 746–754.
[26] H.C. Fiedler, The effect of deformation on the martensitic transformation in austenitic stainless steels, Trans. ASM 47 (1955) 267–290.
[27] J.R. Strife, M.J. Carr, G.S. Ansell, The effect of austenite prestrain above the m d temperature on the martensitic transformation in fe-ni-cr-c alloys, Metall. Mater. Trans. A 8 (9) (1977) 1471–1484.
[28] P.H. Shipway, H.K.D.H. Bhadeshia, The mechanical stabilisation of widmanstätten ferrite, Mater. Sci. Eng., A 223 (1–2) (1997) 179–185.
[29] D.P. Dunne, Formation of ferritic products during continuous cooling of a cu-bearing hsla steel, ISIJ Int. 46 (5) (2006) 759–768.
[30] Francesca G. Caballero, C. Garcia-Mateo, M.J. Santofimia, Michael K. Miller, C. Garcia De Andres, New experimental evidence on the incomplete transformation phenomenon in steel, Acta Mater. 57 (1) (2009) 8–17.
[31] John G. Speer, David V. Edmonds, Fernando C. Rizzo, David K. Matlock, Partitioning of carbon from supersaturated plates of ferrite, with application to steel processing and fundamentals of the bainite transformation, Curr. Opin. Solid State Mater. Sci. 8 (3) (2004) 219–237.
[32] H.K.D.H. Bhadeshia, L.E. Svensson, Modelling the evolution of microstructure in steel weld metal, Math. Model. Weld Phenom. 1 (1993) 109–182.
[33] A. Stern, D. Ashkenazi, D. Cvikel, B. Rosen, E. Galili, Archeometallurgical and technical characterization of 7th century ad iron fishing-spear and fire basket found in the dor lagoon, Israel, J. Archaeol. Sci.Rep. 3 (2015) 132–143.
[34] Matthias Militzer, Phase field modeling of microstructure evolution in steels, Curr. Opin. Solid State Mater. Sci. 15 (3) (2011) 106–115.
[35] Irina Loginova, John Agren, Gustav Amberg, On the formation of widmanstätten ferrite in binary fe–c–phase-field approach, Acta Mater. 52 (13) (2004) 4055–4063.
[36] Akinori Yamanaka, Tomohiro Takaki, Yoshihiro Tomita, Phase-field simulation of austenite to ferrite transformation and widmanstätten ferrite formation in fe-c alloy, Mater. Trans. 47 (11) (2006) 2725–2731.
[37] Wei Yan, Namin Xiao, Yun Chen, Dianzhong Li, Phase-field modeling of widmanstätten ferrite formation during isothermal transformation in low carbon steels, Comput. Mater. Sci. 81 (2014) 503–509.
[38] Maeva Cottura, Benoît Appolaire, Alphonse Finel, Yann Le Bouar, Phase field study of acicular growth: role of elasticity in widmanstätten structure, Acta Mater. 72 (2014) 200–210.
[39] Li Zhang, Yao Shen, Haibo Wan, Xiaochuan Xiong, Lanting Zhang, The study of widmanstätten ferrite in fe–c alloys by a phase field model coupled with anisotropic elasticity, J. Alloys Compd. 650 (2015) 239–247.
[40] Avisor Bhattacharya, Kumar Ankit, Britta Nestler, Phase-field simulations of curvature-induced cascading of widmanstätten-ferrite plates, Acta Mater. 123 (2017) 317–328.
[41] Oleg Tschukin, Alexander Silberzahn, Michael Selzer, Prince GK. Amos, Daniel Schneider, Britta Nestler, Concepts of modeling surface energy anisotropy in phase-field approaches, Geoth. Energy 5 (1) (2017) 19.
[42] T.A. Schroeder, C.M. Wayman, The formation of martensite and the mechanism of the shape memory effect in single crystals of cu-zn alloys, Acta Metall. 25 (12) (1977) 13751383–13811391.
[43] P.S. Kotval, R.W.K. Honeycombe, An fcc- cph transformation in the copper-germanium system, Acta Metall. 16 (4) (1968) 597–607.
[44] HMl Clark, C.M. Wayman, Phase Transformations, vol. 59, ASM, Metals Park, OH, 1970.
[45] H.K.D.H. Bhadeshia, Bcc-bcc orientation relationships, surface relief and displacive phase transformations in steels, Scripta Metall. 14 (7) (1980) 821–824.
[46] H.K.D.H. Bhadeshia, A rationalisation of shear transformations in steels, Acta Metall. 29 (6) (1981) 1117–1130.
[47] John J. Jonas, Youliang He, Gijs Langelaan, The rotation axes and angles involved in the formation of self-accommodating plates of widmanstätten ferrite, Acta Mater. 72 (2014) 13–21.
[48] Vladimir V. Basabe, John J. Jonas, Chiradeep Ghosh, Formation of widmanstätten ferrite in a 0.036% nb low carbon steel at temperatures above the ae3, Steel Res. Int. 85 (1) (2014) 8–15.
[49] H.K.D.H. Bhadeshia, L.-E. Svensson, The microstructure of submerged arc-weld deposits for high-strength steels, J. Mater. Sci. 24 (9) (1989) 3180–3188.
[50] J.R. Yang, L.C. Chang, The effect of stress on the widmanstätten ferrite transformation, Mater. Sci. Eng., A 223 (1–2) (1997) 158–167.
[51] Maeva Cottura, Benoît Appolaire, Alphonse Finel, Yann Le Bouar, Plastic relaxation during diffusion-controlled growth of widmanstätten plates, Scripta Mater. 108 (2015) 117–121.
[52] Vitalii L. Ginzburg, Lev D. Landau, On the theory of superconductivity, Zh. Eksp. Teor. Fiz. 20 (1064–1082) (1950) 35.
[53] Britta Nestler, Harald Garcke, Björn Stinner, Multicomponent alloy solidification: phase-field modeling and simulations, Phys. Rev. 71 (4) (2005), 041609.
[54] Britta Nestler, Phasenfeldmodellierung Mehrphasiger Erstarrung, PhD thesis, Aachen, Ph.D. thesis, 2000.
[55] Johannes Hötzer, Oleg Tschukin, Marouen Ben Said, Marco Berghoff, Marcus Jainta, Georges Barthelemy, Nikolay Smorchkov, Daniel Schneider, Michael Selzer, Britta Nestler, Calibration of a multi-phase field model with quantitative angle measurement, J. Mater. Sci. 51 (4) (2016) 1788–1797.
[56] I. Steinbach, F. Pezzolla, A generalized field method for multiphase transformations using interface fields, Phys. Nonlinear Phenom. 134 (4) (1999) 385–393.
[57] Ingo Steinbach, Phase-field models in materials science, Model. Simulat. Mater. Sci. Eng. 17 (7) (2009), 073001.
[58] Mathis Plapp, Unified derivation of phase-field models for alloy solidification from a grand-potential functional, Phys. Rev. 84 (3) (2011), 031601.
[59] Johannes Hötzer, Marcus Jainta, Philipp Steinmetz, Britta Nestler, Anne Dennstedt, Amber Genau, Martin Bauer, Harald Köstler, Ulrich Rüde, Large scale phase-field simulations of directional ternary eutectic solidification, Acta Mater. 93 (2015) 194–204.
[60] PG Kubendran Amos, L.T. Mushongera, Britta Nestler, Phase-field analysis of volume-diffusion controlled shape-instabilities in metallic systems-i: 2-dimensional plate-like structures, Comput. Mater. Sci. 144 (2018) 363–373.
[61] PG Kubendran Amos, L.T. Mushongera, Tobias Mittnacht, Britta Nestler, Phase-field analysis of volume-diffusion controlled shape-instabilities in metallic systems-ii: finite 3-dimensional rods, Comput. Mater. Sci. 144 (2018) 374–385.
[62] Daniel Schneider, Oleg Tschukin, Abhik Choudhury, Michael Selzer, Thomas Böhlke, Britta Nestler, Phase-field elasticity model based on mechanical jump conditions, Comput. Mech. 55 (5) (2015) 887–901.
[63] Daniel Schneider, Ephraim Schoof, Oleg Tschukin, Andreas Reiter, Christoph Herrmann, Felix Schwab, Michael Selzer, Britta Nestler, Small strain multiphase-field model accounting for configurational forces and mechanical jump conditions, Comput. Mech. 61 (3) (2018) 277–295.
[64] M. Silhavy, The Mechanics and Thermodynamics of Continuous Media, Springer Verlag, 1997.
[65] Bo Sundman, John Agren, A regular solution model for phases with several components and sublattices, suitable for computer applications, J. Phys. Chem. Solid. 42 (4) (1981) 297–301.
[66] T.T. Arif, R.S. Qin, A phase-field model for bainitic transformation, Comput. Mater. Sci. 77 (2013) 230–235.
[67] Per Gustafson, A thermodynamic evaluation of the fe–c system, Scand. J. Metall. 14 (5) (1985) 259–267.
[68] William C. Johnson, J.Iwan D. Alexander, Interfacial conditions for thermomechanical equilibrium in two-phase crystals, J. Appl. Phys. 59 (8) (1986) 2735–2746.
[69] J. Hötzer, A. Reiter, H. Hierl, P. Steinmetz, M. Selzer, Britta Nestler, The parallel multi-physics phase-field framework pace3d, J. Comput. Sci. 26 (2018) 1–12.
[70] Ephraim Schoof, Daniel Schneider, Nick Streichhan, Tobias Mittnacht, Michael Selzer, Britta Nestler, Multiphase-field modeling of martensitic phase transformation in a dual-phase microstructure, Int. J. Solid Struct. 134 (2018) 181–194.
[71] D.A. Porter, K.E. Easterling, Phase Transitions in Metals and Alloys, 1992.
[72] Tae Wook Heo, Long-Qing Chen, Phase-field modeling of displacive phase transformations in elastically anisotropic and inhomogeneous polycrystals,

Acta Mater. 76 (2014) 68–81.
[73] Claas Hüter, Mingxuan Lin, Diego Schicchi, Martin Hunkel, Ulrich Prahl, Robert Spatschek, A multiscale perspective on the kinetics of solid state transformations with application to bainite formation, AIMS Mater. Sci. 2 (4) (2015) 319–345.
[74] A.G. Khachaturyan, Theory of Structural Transformations in Solids, 1983.
[75] Efim A. Brener, V.I. Marchenko, R. Spatschek, Influence of strain on the kinetics of phase transitions in solids, Phys. Rev. 75 (4) (2007), 041604.
[76] A. Van der Ven, L. Delaey, Models for precipitate growth during the $\gamma \rightarrow \alpha + \gamma$ transformation in fe-c and fe-c-m alloys, Prog. Mater. Sci. 40 (3) (1996) 181–264.
[77] S.A. Mujahid, H.K.D.H. Bhadeshia, Coupled diffusional/displacive transformations: effect of carbon concentration, Acta Metall. Mater. 41 (3) (1993) 967–973.
[78] Yongjoon Kang, Seonghoon Jeong, Joo-Hee Kang, Changhee Lee, Factors affecting the inclusion potency for acicular ferrite nucleation in high-strength steel welds, Metall. Mater. Trans. A 47 (6) (2016) 2842–2854.
[79] G.P. Ivantsov, et al., Gp ivantsov, dokl. akad. nauk sssr, in: Dokl. Akad. Nauk SSSR, vol. 58, 1947, p. 567.
[80] D. Pilipenko, E.A. Brener, C. Hüter, Theory of dendritic growth in the presence of lattice strain, Phys. Rev. 78 (6) (2008), 060603.
[81] Christoph Herrmann, Ephraim Schoof, Daniel Schneider, Felix Schwab, Andreas Reiter, Michael Selzer, Britta Nestler, Multiphase-field model of small strain elasto-plasticity according to the mechanical jump conditions, Comput. Mech. (2018) 1–14.
[82] O. Tschukin, D. Schneider, B. Nestler, An elasto-chemical phase-field model for isotropic solids, European Journal of Mechanics-A/Solids, Eur. J. Mech. A/Solids (2018).